Compact MIMO Antenna OTA Measurement System with Utilization of Metasurface for Wavefront Manipulator

Jinhyun Kim, *Graduate Student Member, IEEE* and Uichan Park, *Student Member, IEEE*, Haeseung Lee, *Member, IEEE*, Kyungho Yoo, *Senior Member, IEEE*, and Jungsuek Oh, *Senior Member, IEEE*

***Abstract*—A novel application of the metasurface for minimizing the Sub-6 GHz MIMO antenna measurement system is proposed. To reduce measurement errors across frequencies and within the measurement system, an active transmit-type metasurface based on the PIN diode is adopted, enabling compensation for phase without amplitude variation. Moreover, the unit cell is designed with a size of 20 mm $\times$ 20 mm ($0.25\lambda \times 0.25\lambda$) to reduce quantization loss. The Mean Square Error (MSE) of the E-field is calculated to verify wavefront uniformity. The paper introduces a measurement method that can determine quiet-zone generation instead of relying on antenna probe measurements. This method utilizes path loss changes per unit distance. Based on the path loss difference measurement results, the metasurface can form a quiet zone approximately 30% closer to the receiver antenna. Additionally, it is confirmed that the proposed system can minimize measurement error by reconfiguring the metasurface across frequency variations.**

***Index Terms*—Antenna measurement system, Metasurface, Transmit array, Sub-6 GHz Massive MIMO**

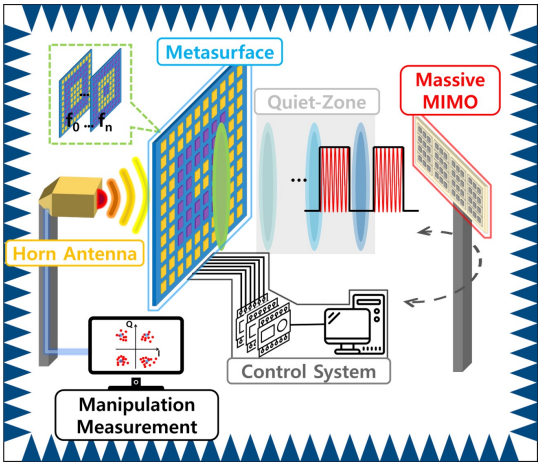

Fig. 1: Diagram of the proposed MIMO antenna measurement system.

I. Introduction

The Massive Multiple-Input Multiple-Output (Massive MIMO) antenna is an emerging wireless communication device gaining prominence as a crucial antenna design in 5G communication at base stations [1]–[5]. The MIMO antenna utilizes multiple antennas and RF chains to communicate with multiple users, offering high gain. However, communication performance can be adversely affected by variations in the amplitude and phase of the input RF signal due to cables, connectors, and thermal issues. Therefore, it is crucial to measure the MIMO antenna in practical Over-the-Air (OTA) conditions to accurately assess its performance.

However, MIMO antennas generally have a large aperture size, resulting in a far-field condition defined by the Fraunhofer distance that extends significantly farther [6]–[8]. Such a system requires high-quality equipment to address path loss issues, where the signal-to-noise ratio (SNR) plays a critical role in maintaining sufficient levels. Additionally, minimizing scatter, including reflection, refraction, and diffraction, is vital for accurately measuring MIMO performance. This requirement calls for the use of tremendous absorbers, leading to increased construction costs for the measurement system.

Because of the aforementioned problems, considerable research has been undertaken to minimize the MIMO antenna measurement system. One proposed solution is the near-field-to-far-field (NF-FF) transformation, where the Antenna Under Test (AUT) is measured for magnitude and phase in the near field using antenna probes [9]–[12]. Based on these measurements, far-field patterns are calculated through the NF-FF transformation. However, this method demands numerous probe antennas (probe wall) and involves time-consuming scanning [11], [12]. Furthermore, it can only measure a single frequency per scanning and cannot estimate the modulated signal.

Another approach to reducing the measurement system is to reconstitute the electromagnetic wave by controlling the wavefront [13]–[24].By shaping the wavefront, phase can be distributed uniformly, resembling the far-field condition. From this perspective, the Compact Antenna Test Range (CATR) has been proposed to reduce the antenna measurement system using a reflective passive metasurface. While this method successfully decreases the size of the measurement system, it does not enable phase compensation adjustments across frequencies, making accurate measurements impossible. Additionally, the large reflector size creates challenges in minimizing the measurement environment [15]–[18].

The transmit-type metasurface can also reconfigure the wavefront through unit cell control, prompting extensive research into its use in antenna measurement systems [19]–[21].

Manuscript received. This work was supported by Samsung Electronics Global Technology Center (50%), and Institute of Information & communications Technology Planning & Evaluation (IITP) grant funded by the Korea government (MSIT) (No.2021-0-00763, Innovative Fusion Technologies of Intelligent Antenna Material/Structure/Network for THz 6G, 50%). (Corresponding Author : Jungsuek Oh)

J. Kim, U. Park, and J. Oh are with the Department of Electrical and Computer Engineering (ECE), Institute of New Media and Communications (INMC), Seoul National University, Seoul 151-742, Republic of Korea (e-mail:jungsuek@snu.ac.kr).

H. Lee, and K. Yoo are with the Global Technology Research, Samsung Electronics, Co. Ltd, Suwon, Republic of Korea (e-mail:hs0322.lee@samsung.com).

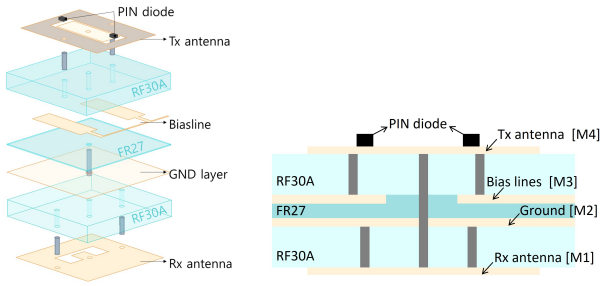

(a) (b)

Fig. 2: Proposed unit cell structure (a) unit cell structure perspective view (b) Cross-section view of the designed unit cell.

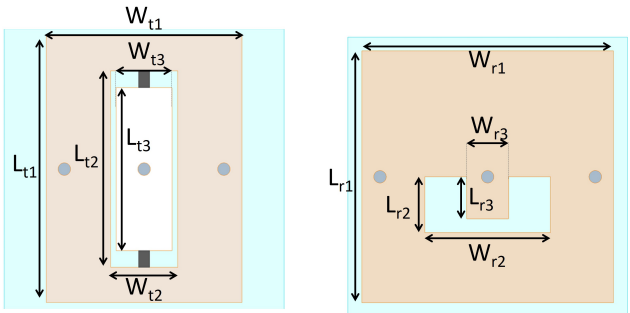

(a) (b)

Fig. 3: Geometry of the proposed unit cell design (a) unit cell top view (b) unit cell bottom view.

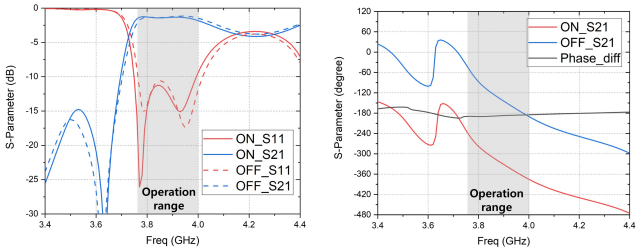

(a) (b)

Fig. 4: Unit cell S-parameter simulation results along the diode states (a) S11 and S21 magnitude simulation results along the diode states (b) S21 phase results along the diode states.

Although passive metasurfaces can modulate the wavefront with minimal quantization loss, they exhibit non-uniform amplitude across different unit cell types and cannot adjust to frequency variations. As a result, the passive metasurface functions well as a wavefront manipulator at a single frequency, but measurement errors increase at other frequencies.

In this work, a method for minimizing the antenna measurement system using the active transmit-type metasurface is proposed to address measurement system problems. As shown in Fig. 1, the active metasurface functions as a wavefront manipulator, allowing the formation of a wavefront equivalent to the far-field condition. As a result, a successfully implemented miniaturized MIMO measurement system capable of measuring modulated signals is achieved.

II. Design of the Wavefront Manipulator

A. Wavefront Manipulator Design

In order to utilize the metasurface as a wavefront manipulator in an antenna measurement system, it is essential that only the phase is controlled according to the operation of the manipulator, regardless of the magnitude. Furthermore, magnitude and phase variations should be maintained across frequencies despite the manipulator control. Unlike other reconfigurable components, such as liquid crystal and varactor, the PIN diode base unit cell enables compensation of phase with the same amplitude variation by adjusting the direction of the current. Therefore, the unit cell is designed with a PIN diode to manipulate the wavefront. The unit cell design is proposed in Fig. 2. In Fig. 2(a), the unit cell comprises a U-slot antenna (Rx antenna), ground layer, biasline layer, and O-slot antenna (Tx antenna) with two diodes. As shown in Fig. 2(b), Taconic RF-35 (ϵ_r = 2.97, $\tan\delta = 0.0013$), which has a height of 1.52 mm, is selected as the substrate, and the two substrates are attached to each other with prepreg, which is FR27 (ϵ_r = 2.72, $\tan\delta = 0.0014$), with a thickness of 0.14 mm.

Rx antenna is designed as a U-slot antenna to increase bandwidth and form a electrical potential zero point. The point is connected to the ground layer to apply the voltage for operating the PIN diode in the Tx antenna. Rx antenna is connected to Tx antenna by vias to deliver the signal and apply DC ground voltage. To minimize the complexity of the manipulator control system, the DC voltage is applied to the ground layer. Therefore, the PIN diodes can be controlled without negative voltage by biasing the control voltage to be higher and lower than the DC ground voltage. As shown in Fig. 3(a), the O-slot antenna is utilized as the Tx antenna, with two PIN diodes, BAR50-02V, mounted in opposite directions along the central via. Consequently, depending on the control voltage, one diode is always turned ON while the other is turned OFF. In this paper, the condition where the diode positioned at the top is turned ON is defined as the ON state, while the condition where it is turned OFF is defined as the OFF state. Under these conditions, the signal path from the Rx antenna is altered according to the diode's operation, thereby enabling a 180-degree phase difference in the unit cell's state, as illustrated in Fig. 4(b). To control the PIN diodes, the biasline is implemented in the M3 metal layer. To minimize the biasline effect, a large pad is included in the bias network to achieve the virtual ground.

The unit cell is designed using Floquet port simulation with

TABLE I: wavefront manipulator unit cell dimensions parameter

Tx antenna	Values [mm]	Rx antenna	Values [mm]
W_{t1}	14.5	W_{r1}	18
W_{t2}	5.3	W_{r2}	6.5
W_{t3}	3	W_{r3}	2.5
L_{t1}	19.1	L_{r1}	18
L_{t2}	13.2	L_{r2}	5.5
L_{t3}	2.5	L_{r3}	4

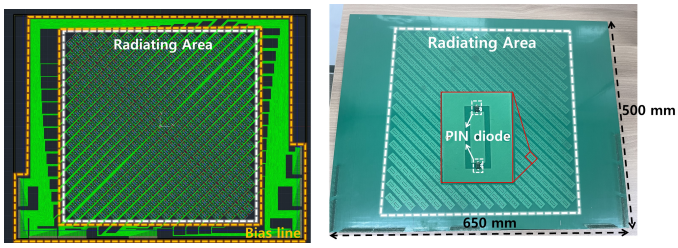

(a) (b)

Fig. 5: The photograph of the proposed wavefront manipulator (a) Diagram of the proposed wavefront manipulator (b) Top view of the fabricated proposed wavefront manipulator.

the Ansys HFSS software. The S-parameter simulation was performed in the horizontal direction, where current flows through the diode, thereby aligning with the Tx antenna's polarization. The geometry diagram of the unit cell is illustrated in Fig. 3 and the detailed dimension parameters are shown in Table I. In the proposed system, the metasurface is utilized as the wavefront manipulator, so quantization loss should be minimized. Typically, when designing a metasurface, the size of the unit cell is $0.5\lambda \times 0.5\lambda$. However, the proposed wavefront manipulator targets practical systems by minimizing quantization loss. In practical MIMO antenna systems, each telecommunication operator typically uses around 100 MHz of bandwidth [25]. Therefore, the wavefront manipulator unit cell was designed to be $0.25\lambda \times 0.25\lambda$ to maximize wavefront uniformity and minimize quantization error.

The S-parameter simulation results are demonstrated in Fig. 4. The diode is modeled as a lumped component consisting of resistance and capacitance, R_{on} and C_{off}. Based on Fig. 4(a), the S_{11} value determines the -10 dB bandwidth of the unit cell to be 250 MHz, and the insertion loss is maintained around -1.5 dB within this bandwidth, regardless of the unit cell operation. Within the same bandwidth, the phase difference of the unit cell across the diode states is maintained at approximately 180°, as indicated in Fig. 4(b).

The fabricated manipulator is shown in Fig. 5. The manipulator utilizes 420 unit cells, and the size of the manipulator with the bias network is 500 mm × 650 mm, which includes an effective radiating aperture of size 420 mm × 420 mm. To maximize the radiating area, the width and spacing of the bias lines were set to the minimum feasible distance of 100 µm. The proposed wavefront manipulator is designed for use with the MIMO antenna measurement system. Generally, the MIMO antenna has a 45° slant polarization to improve channel conditions through fading [26]–[28]. The unit cell has linear polarization. Therefore, the unit cell arrangement is also inclined to match the MIMO antenna polarization. Moreover, since the wavefront manipulator is used to minimize the antenna measurement system, the focal length of the wavefront manipulator should be carefully considered. Taper efficiency and spillover efficiency respectively indicate how uniformly the E-field is incident on the metasurface and how much it spreads along the edges. If the focal length is too short, the phase variation becomes excessive, making proper phase compensation difficult. Conversely, if the focal length is too long, not only does the measurement setup become larger, but the E-field also propagates beyond the metasurface aperture, making phase compensation impossible. Therefore, it is essential to determine a suitable focal length so that compensation can be applied for a sufficiently uniform phase distribution while also creating a quiet zone within a minimized measurement system.

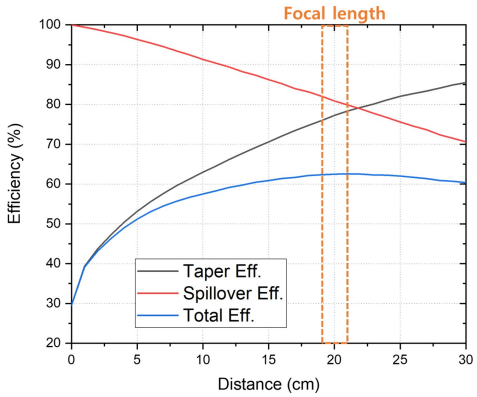

Fig. 6: Calculated result of the wavefront manipulator efficiency along the focal length.

Due to the reason, focal length is calculated based on the taper and spillover efficiencies by below equations [29].

$$\eta_{taper} = \frac{1}{A}\frac{|\iint_A I dA|^2}{\iint_A |I|^2 dA} \tag{1}$$

$$\eta_{spillover} = \frac{\iint_A \vec{S} \cdot d\vec{A}}{P_{rad}} \tag{2}$$

$$\eta_{Total} = \eta_{taper} \times \eta_{spillover} \tag{3}$$

The aperture dimension, E-field intensity, Poynting vector, and radiated power to manipulator are represented by A, I, S, and P_{rad}, and the calculation results is shown in Fig. 6. Therefore, the focal length of the metasurface is set to 20 cm for the maximum total efficiency.

B. Wavefront Manipulation with Metasurface

To verify the phase modulation achieved by the proposed metasurface application, the compensation of the wavefront manipulator focuses on minimizing the magnitude and phase mean squared error (MSE) calculated based on the equations below.

$$MSE_{mag} = \int_{A_{Quiet}} \frac{(E_{Mag} - E_{Mag\_avg})^2}{A_{Quiet}} \tag{4}$$

$$MSE_{phase} = \int_{A_{Quiet}} \frac{(E_{Phase} - E_{Phase\_avg})^2}{A_{Quiet}} \tag{5}$$

Based on the equations (4), (5), the electrical magnitude and phase uniformity of the quiet zone can be calculated. A_{quiet} is defined as the target area for uniformity measurement, and the average electric field magnitude, E_{mag_avg}, and phase, E_{phase_avg}, are calculated within this area. The difference between each point's electric field magnitude and phase and their

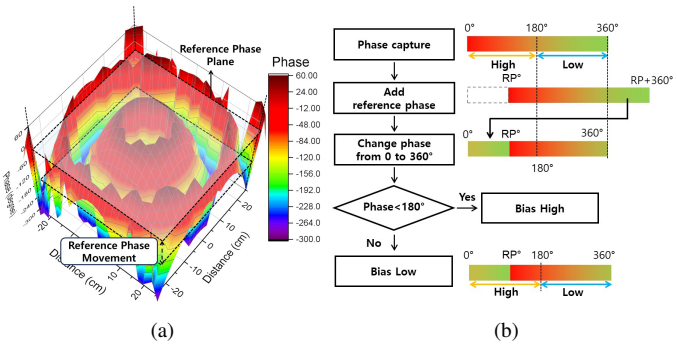

(a) (b)

Fig. 7: The concept of the reference phase (a) Diagram representing the concept of the reference phase (b) Flow chart of the phase compensation.

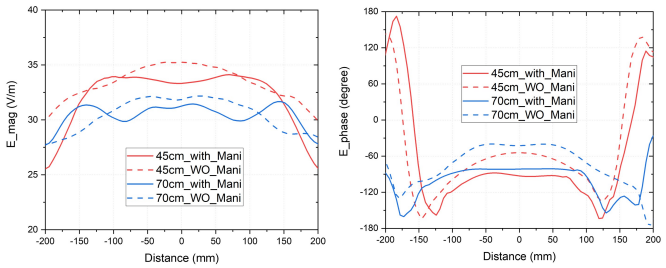

(a) (b)

Fig. 8: E-field distribution simulation results along the distance by the wavefront manipulator operation. (a) E-field magnitude distribution (b) E-field phase distribution.

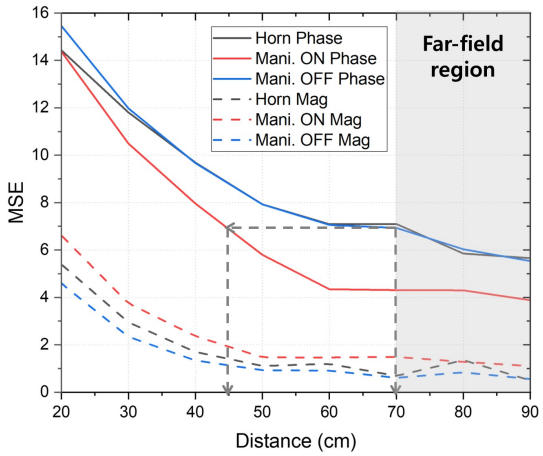

Fig. 9: MSE calculation results along the distance by the wavefront manipulator operation.

respective averages is then determined, and the resulting error indicates the uniformity of both the magnitude and phase of the electric field. The proposed wavefront manipulator utilizes PIN diodes to minimize the variation in the magnitude of the E-field due to the operation of the metasurface. Therefore, to minimize the quantization loss of the wavefront manipulator, the control bias setting with the minimum MSE was obtained by controlling the manipulator through the reference phase.

The concept of the reference phase is shown in Fig. 7. The proposed wavefront manipulator experiences quantization loss due to the size of the unit cells. Moreover, the proposed unit cell performs phase compensation through current path control. However, ideal phase compensation is not achievable. Consequently, the phase is compensated using values that most closely approximate the necessary compensation to form a uniform wavefront. Therefore, even with phase compensation, the uniformity of the wavefront can vary depending on the reference phase. For this reason, a concept of the reference phase to minimize quantization error is proposed in this paper. As illustrated in Fig. 7(a), the wavefront manipulator compensates the phase according to the reference phase, resulting in changes to the MSE.

The phase compensation of the manipulator with regard to the reference phase is described in Fig. 7(b). The proposed wavefront manipulator operates by controlling the current path through the PIN diode, so it enables to allow 180° phase control. Therefore, phases below 180° are compensated through the unit cell, and phases above 180° are not compensated by setting the unit cell to the OFF state. At this point, the range of phase compensation based on the reference phase is modified by adjusting the phase range that requires compensation by incorporating the reference phase. Therefore, different phase compensation configurations can be applied to the wavefront manipulator according to the reference phase, allowing the determination of the phase compensation distribution that provides the highest wavefront uniformity.

Based on Fig. 7(b), the manipulator controls the wavefront, and the magnitude and phase distribution of the E-field are illustrated in Fig. 8. Fig. 8 shows the simulation results for the magnitude and phase distribution of the E-field with and without manipulation at 45 cm and 70 cm using a normal horn antenna. The magnitude and phase distribution of the manipulated E-field at 45 cm exhibit a similar pattern to the non-manipulated E-field at 70 cm.

Moreover, the MSE variation over distance depending on the manipulator operation is shown in Fig. 9. The MSE was calculated for an area of 420 mm $\times$ 420 mm, which corresponds to the effective radiating aperture of the wavefront manipulator and represents 50% of its total area. "Mani. ON" represents the manipulator performing phase compensation, while "Mani. OFF" indicates that all unit cells are controlled in the same state, resulting in no phase compensation. When only the horn antenna is present, the far-field condition, based on the Fraunhofer far-field calculation, begins at a distance of 70 cm. The far-field generation point determined by phase MSE appears to align with that of the uncontrolled manipulator. However, with the manipulator controlling the wavefront, the same phase MSE point is achieved at a reduced distance of 45 cm, approximately 35% shorter than the horn antenna's far-field condition. The manipulator compensates the phase without affecting the magnitude, enabling a point of similar phase uniformity to form closer to the wavefront manipulator.

As shown in Fig. 10, the point of E-field uniformity is observed much closer to the Rx horn antenna when the wavefront manipulator is operating. Therefore, it can be concluded that the metasurface based wavefront manipulator effectively generates the quiet zone closer to the Rx antenna.

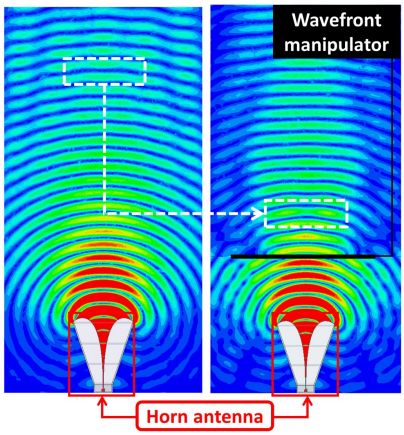

Fig. 10: Electric field distribution graph along the wavefront manipulator appearance.

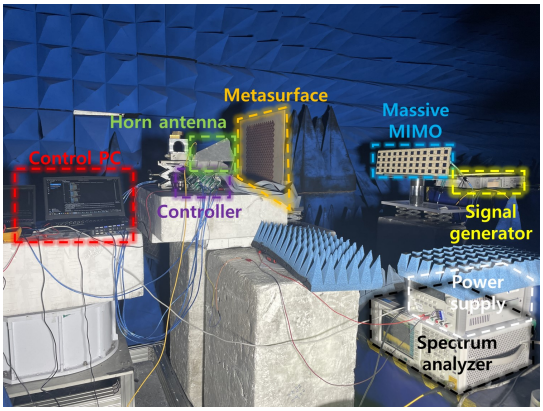

Fig. 11: The photograph of the MIMO measurement system.

III. Measurement

To verify the application of the metasurface as the wavefront manipulator in this paper, the measurement setup is shown in Fig. 11. The Keysight vector signal generator E4438 and signal analyzer N9020A were used to measure, and 9 Arduino MEGA 2560 and DC power supply E3634A were utilized to control the wavefront manipulator using Python. The Tx antenna is a massive MIMO antenna, and the Rx antenna is a DRH-020-180 dual-ridged antenna fabricated in the Microwave Technologies Group (MTG). The massive MIMO antenna deployed in practical telecommunications systems was employed. One MIMO antenna unit consists of four sub-arrays, each formed by three antenna elements. Every antenna element is configured with a 45° slant polarization, with the two orthogonal polarizations serving as the Tx and Rx antennas, respectively. Generally, to verify the formation of a quiet zone, the magnitude and phase of the E-field at each point are measured using an antenna probe. The uniformity of the wavefront is calculated by comparing the magnitude and phase between adjacent points to determine the quiet zone. However, this method not only requires an antenna probe but also incurs high costs in terms of time and computing resources. Therefore, this paper proposes a method to verify the formation of a quiet zone by analyzing the variation in path loss per unit distance. Under far-field conditions, when the wavefront forms a plane wave shape, the magnitude and phase of the E-field are uniform, and this E-field is denoted as E_{uni}. However, in the near-field, the wavefront becomes non-uniform, which is referred to as $E_{non-uni}$, and the resulting error is denoted as E_{error}. The E_{error} is defined as (6).

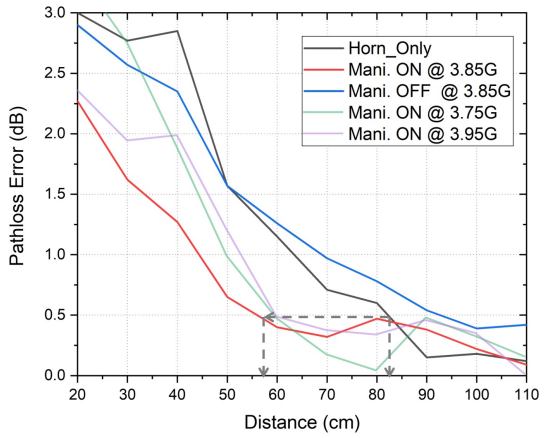

Fig. 12: The graph of pathloss difference measurement along the wavefront manipulator operation.

$$E_{non-uni} = E_{uni} + E_{error} \tag{6}$$

The power received by the Rx antenna, P_{meas}, is related as follows:

$$\begin{aligned} P_{\text{meas}} &\propto \left(E_{\text{non-uni}}\right)^2 \\ &\propto \left|E_{\text{uni}}\right|^2 + 2\,Re\left(E_{\text{uni}} \cdot E_{\text{error}}^*\right) + \left|E_{\text{error}}\right|^2 \end{aligned} \tag{7}$$

When defining ΔPL as the path loss error caused by the non-uniformity of the wavefront, it can be expressed as below.

$$\begin{aligned} \Delta PL &\propto 10\log\left(\frac{P_{\text{meas}}}{P_{\text{uni}}}\right) \\ &\propto 10\log\left(1 + \frac{2\,Re\left(E_{\text{uni}}E_{\text{error}}^*\right)}{\left|E_{\text{uni}}\right|^2} + \frac{\left|E_{\text{error}}\right|^2}{\left|E_{\text{uni}}\right|^2}\right) \end{aligned} \tag{8}$$

Therefore, when the wavefront is non-uniform, E_{error} increases, leading to an increase in ΔPL. Consequently, the change in path loss per unit distance represents the uniformity of the wavefront, and an increase in the change in path loss indicates a decrease in the uniformity of the wavefront.

In a far-field condition with a uniform wavefront, the path loss remains consistent over unit distances, resulting in minimal differences in path loss. Conversely, if the wavefront is not uniform, the path loss difference per unit distance is inconsistent. By measuring the path loss as the Rx antenna moves over unit distances and analyzing the differences, it is possible to confirm the quiet zone and far-field conditions. The path loss measurement results are shown in Fig. 12. When the MIMO antenna is positioned close to the Rx antenna, the absolute value of the path loss difference increases. This means that the uniformity of the wavefront is degraded. Based on the path loss difference, the far-field distance of the horn antenna is about 82 cm, and the average path loss difference is about 0.5 dB per 10 cm in the measurement setup. The path loss variation for the horn antenna alone, referred to as Horn_Only,

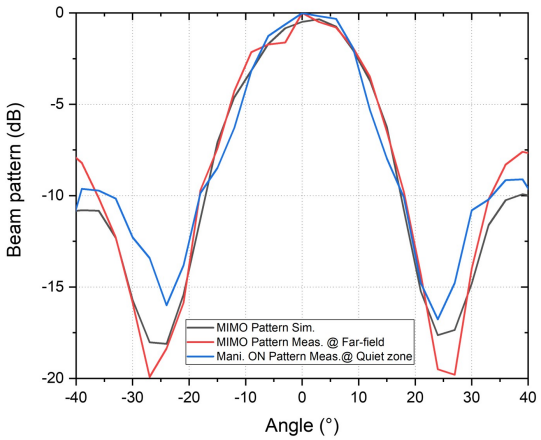

Fig. 13: The beampattern measurement result along the wavefront manipulator operation.

and the path loss error for the wavefront manipulator without phase compensation both show errors exceeding 0.5 dB at approximately 82 cm and 92 cm, respectively. On the other hand, when the wavefront manipulator is phase compensated, the point where the change in path loss variation exceeds 0.5 dB is closer to the Rx, around 57 cm. Although there is an error of about 10 cm compared to the MSE simulation result, it can be concluded that the quiet zone can be formed close to the Rx using the operation of the wavefront manipulator.

Based on the path loss error measurement results, the wavefront manipulator can generate the quiet zone closer to the Rx system, so the beam pattern of the MIMO antenna was also measured in the quiet zone and far-field. As shown in Fig. 13, the measured MIMO antenna beam pattern is similar to the simulation beam pattern result. For the beam pattern measured in the quiet zone, it seems that even though the side lobe level is slightly different from the far field result, the null point and half-power beam width are similar to the far field beam pattern. Therefore, it can be concluded that the performance of the MIMO antenna can be verified by measuring at a much closer distance than the far field measurement through the operation of the proposed wavefront manipulator.

It is confirmed that the proposed wavefront manipulator effectively forms the quiet zone, allowing the MIMO antenna to be verified at a close distance rather than in the far field by measuring the path loss difference and beam pattern. Therefore, the proposed measurement system can be adopted for modulated signal measurement. In Fig. 14, error vector modulation (EVM) measurement results are illustrated. To measure the EVM, the LTE 16-QAM signal with a 20 MHz bandwidth is utilized at distances of 55 cm and 90 cm, and the wavefront manipulator is operated to compensate for the 3.85 GHz signal.

According to Fig. 14, the EVM measurement results in the quiet zone and far field exhibit an error of less than 1%, providing 95% reliability based on 3GPP far-field measurement uncertainty [30]. However, the fixed wavefront manipulator operates within a bandwidth of approximately 3.825 GHz to 3.88 GHz, which is 55 MHz. Consequently, the wavefront manipulator cannot ensure 95% confidence due to the EVM error, making the EVM measurements in the quiet zone unreliable.

TABLE II: Performance Comparison with the State-of-the-art Metasurface

Ref	Type	Freq (GHz)	N. Sub layer	F/D	Aperture size (mm)	EVM Meas.	QZ size (mm)
[18]	Passive	28	1	1.83	177×189	X	100×100
[19]	Passive	2.6	5	0.287	502×502	X	255×255
[21]	Passive	26	1	1.1	400×400	X	200×200
[22]	Active	18	1	N.A.	131×131	X	N.A.
[23]	Passive	26	3	0.7	550×550	X	200×200
[24]	Passive	1.8	1	1.17	600×600	X	500×500
[31]	Active	28	1	1.2	45.4×45.4	X	N.A.
[32]	Active array	5	N.A.	1.4	550×550*	X	200×200
This work	Active	3.85	2	0.476	420 × 420	O	420×420

*: Estimate from the paper

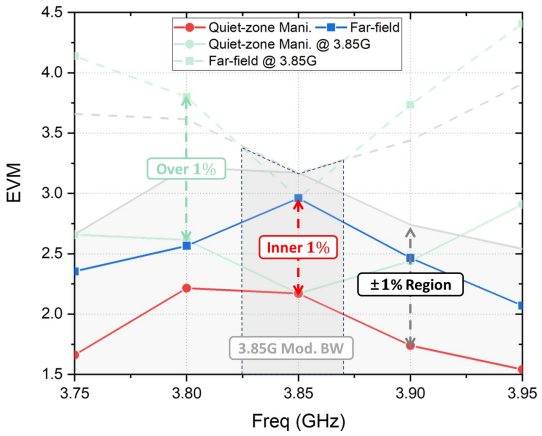

Fig. 14: The EVM measurement result along the wavefront manipulator operation.

Therefore, the wavefront manipulator should be designed as an active type that can be reconfigured through bias control to adjust phase compensation according to the measurement frequency. By operating the wavefront manipulator in 50 MHz steps, EVM results with over 95% confidence can be achieved in the quiet zone across the 3.75 GHz to 3.95 GHz range, as shown in Fig. 14. In Table II, the performance of the proposed waveform manipulator is summarized and compared with that of other published work. As shown in Table II, the proposed system has a very low F/D ratio while forming a wide quiet zone. In addition, the EVM measurement proves the superiority of the proposed system while requiring variable characteristics. This demonstrates that the proposed metasurface-based wavefront manipulator can minimize the measurement environment by reducing the quiet zone generation point through frequency-dependent phase compensation. Additionally, it verifies that the modulation signal can be accurately measured in a short-distance quiet zone, and the frequency-reconfigurable wavefront manipulator can provide more precise measurement results for the modulation signal.

IV. Conclusion

This paper proposes the use of a metasurface as a wavefront manipulator to minimize the MIMO antenna measurement system. The unit cell, designed with two diodes, changes the phase by switching the current path without amplitude variation. The unit cell size is $0.25\lambda \times 0.25\lambda$ to minimize quantization loss, and the focal length is determined based

on taper and spillover efficiency. E-field magnitude and phase MSE are calculated for a 50% aperture ratio to verify wavefront uniformity. The wavefront manipulator generates a quiet zone closer to the receiver antenna. Path loss difference over the same interval confirms the quiet zone, eliminating the need for an antenna probe. Results show that the quiet zone forms at a shorter distance with the wavefront manipulator, minimizing the MIMO antenna measurement system. EVM measurements verify that different phase compensation arrangements are required for reliable EVM measurements in the quiet zone at different frequencies. The proposed active wavefront manipulator compensates the phase with constant amplitude variation, further minimizing the MIMO antenna measurement system and enabling reliable measurement results by reconfiguring phase compensation according to frequency. This application of the metasurface as a wavefront manipulator significantly contributes to the development of MIMO antennas.

REFERENCES

[1] E. G. Larsson, O. Edfors, F. Tufvesson, and T. L. Marzetta, "Massive MIMO for next generation wireless systems," *IEEE Commun. Mag.*, vol. 52, no. 2, pp. 186–195, 2014.

[2] A. O. Martínez, J. Ø. Nielsen, E. De Carvalho, and P. Popovski, "An Experimental Study of Massive MIMO Properties in 5G Scenarios," *IEEE Trans. Antennas Propag.*, vol. 66, no. 12, pp. 7206–7215, 2018.

[3] T. E. Bogale and L. B. Le, "Massive MIMO and mmWave for 5G Wireless HetNet: Potential Benefits and Challenges," *IEEE Veh. Technol. Mag.*, vol. 11, no. 1, pp. 64–75, 2016.

[4] L. S. C. Z. L. G. Dong Guiting, Huang Jianlin, "A Compact Dual-Band MIMO Antenna for Sub-6 GHz 5G Terminals," *J. Electromagn. Eng. Sci*, vol. 22, no. 5, pp. 599–607, 2022. [Online]. Available: https://www.jees.kr/journal/view.php?number=3552

[5] K. S. Park Sion, "A Coupled-Fed Broadband Dual-Polarized Magnetoelectric Dipole Antenna for WLAN and Sub-6 GHz 5G Communication Applications," *J. Electromagn. Eng. Sci*, vol. 23, no. 1, pp. 75–77, 2023. [Online]. Available: https://www.jees.kr/journal/view.php?number=3572

[6] K. T. Selvan and R. Janaswamy, "Fraunhofer and Fresnel Distances : Unified derivation for aperture antennas." *IEEE Antennas Propag. Mag.*, vol. 59, no. 4, pp. 12–15, 2017.

[7] M. Chung, L. Liu, A. Johansson, M. Nilsson, O. Zander, Z. Ying, F. Tufvesson, and O. Edfors, "Millimeter-Wave Massive MIMO Testbed with Hybrid Beamforming," in *Conf. Rec. Asilomar Conf. Signals Syst. Comput. (ACSSC)*, 2020, pp. 309–313.

[8] L. S. C. Z. L. G. Dong Guiting, Huang Jianlin, "A Compact Dual-Band MIMO Antenna for Sub-6 GHz 5G Terminals," *J. Electromagn. Eng. Sci*, vol. 22, no. 5, pp. 599–607, 2022. [Online]. Available: https://www.jees.kr/journal/view.php?number=3552

[9] T. K.-O. D. Ulm and T. Schrader, "Antenna calibration based on near-field to far-field transformation algorithms," in *Proc. 13th Eur. Conf. Antennas Propag. (EuCAP)*, 2019, pp. 1–4.

[10] H.-T. Chou, P. H. Pathak, S.-C. Tuan, and R. J. Burkholder, "A Novel Far-Field Transformation via Complex Source Beams for Antenna Near-Field Measurements on Arbitrary Surfaces," *IEEE Antennas Propag. Mag.*, vol. 65, no. 12, pp. 7266–7279, 2017.

[11] H. Gao, W. Wang, Y. Wu, Y. Liu, and G. F. Pedersen, "A Virtual Over-the-Air Method for 5G Massive MIMO Base Station Testing With Flexible Virtual Probes," vol. 7, 2019, pp. 108 474–108 485.

[12] P. Kyösti, W. Fan, and J. Kyröläinen, "Assessing measurement distances for OTA testing of massive MIMO base station at 28 GHz," in *Proc. 11th Eur. Conf. Antennas Propag. (EUCAP*, 2017, pp. 3679–3683.

[13] P. Mei, Y. Cai, K. Zhao, Z. Ying, G. F. Pedersen, X. Q. Lin, and S. Zhang, "On the Study of Reconfigurable Intelligent Surfaces in the Near-Field Region," *IEEE Antennas Propag. Mag.*, vol. 70, no. 10, pp. 8718–8728, 2022.

[14] C. Granet, M. Zhou, S. B. Sørensen, K. W. Smart, J. S. Kot, and J. Ness, "Reflectarray Compact Antenna Test Range Concept," in *2019 13th European Conference on Antennas and Propagation (EuCAP)*, 2019, pp. 1–5.

[15] L. M. Tancioni, A. Jernberg, P. Noren, A. Giacomini, A. Scannavini, L. Foged, R. Braun, M. Boumans, F. Hirn, B. Horrocks, and C. Schröter, "Over-the-Air testing of Active Antenna System Base Stations in Compact Antenna Test Range," in *Proc. 13th Eur. Conf. Antennas Propag. (EuCAP)*, 2019, pp. 1–5.

[16] C. Zhou, Z. Xie, B. Zhang, T. Lei, Z. Li, L. Du, and X. Yuan, "Reconfigurable dielectric metasurface for active wavefront modulation based on a phase-change material metamolecule design," *Opt. Express*, vol. 28, no. 25, pp. 38 241–38 251, Dec 2020. [Online]. Available: http://opg.optica.org/oe/abstract.cfm?URI=oe-28-25-38241

[17] A. Lonnqvist, T. Koskinen, J. Hakli, J. Saily, J. Ala-Laurinaho, J. Mallat, V. Viikari, J. Tuovinen, and A. Raisanen, "Hologram-based compact range for submillimeter-wave antenna testing," *IEEE Antennas Propag. Mag.*, vol. 53, no. 10, pp. 3151–3159, 2005.

[18] A. F. Vaquero, M. Arrebola, M. R. Pino, R. Florencio, and J. A. Encinar, "Demonstration of a reflectarray with near-field amplitude and phase constraints as compact antenna test range probe for 5g new radio devices," *IEEE Trans. Antennas Propag.*, vol. 69, no. 5, pp. 2715–2726, 2021.

[19] J. Tang, X. Chen, X. Meng, Z. Wang, Y. Ren, C. Pan, X. Huang, M. Li, and A. A. Kishk, "Compact Antenna Test Range Using Very Small F/D Transmitarray Based on Amplitude Modification and Phase Modulation," *IEEE Trans. Instrum. Meas.*, vol. 71, pp. 1–14, 2022.

[20] Q. Wei, L. Huang, T. Zentgraf, and Y. Wang, "Optical wavefront shaping based on functional metasurfaces," *Nanophotonics*, vol. 9, no. 5, pp. 987–1002, 2020. [Online]. Available: https://doi.org/10.1515/nanoph-2019-0478

[21] Y. Zhang, Z. Wang, Y. Ren, C. Pan, J. Zhang, L. Jia, and X. Zhu, "A novel metasurface lens design for synthesizing plane waves in millimeter-wave bands," *Electronics*, vol. 11, no. 9, 2022. [Online]. Available: https://www.mdpi.com/2079-9292/11/9/1403

[22] L. Zhang, T. Wang, F. Wang, Y. Liu, and X. Wu, "Programmable metasurface applied to antenna measurement," *Electronics Letters*, vol. 55, no. 13, pp. 726–729, 2019. [Online]. Available: https://ietresearch.onlinelibrary.wiley.com/doi/abs/10.1049/el.2019.0935

[23] Y. Zhang, Z. Wang, Z. Xue, Y. Zhu, and Y. Ren, "A novel metasurface lens antenna design for over-the-air testing in millimetre wave radio resource management measurement," *IET Microw. Antennas Propag.*, vol. 17, no. 6, pp. 434–442, 2023. [Online]. Available: https://ietresearch.onlinelibrary.wiley.com/doi/abs/10.1049/mia2.12352

[24] H. S. Park, Y. J. Song, K. H. Cha, and S. K. Hong, "Effective Plane Wave Generator Based on Reference Field Shaping Using Super-Gaussian Distribution," *IEEE Antennas Wireless Propag. Lett.*, vol. 23, no. 7, pp. 2061–2065, 2024.

[25] M. Massaro and S. Kim, "Why is South Korea at the forefront of 5G? Insights from technology systems theory," *Telecommunications Policy*, vol. 46, no. 5, p. 102290, 2022. [Online]. Available: https://www.sciencedirect.com/science/article/pii/S0308596121001944

[26] Q. Yang, S. Gao, Q. Luo, L. Wen, Y.-L. Ban, X.-X. Yang, X. Ren, and J. Wu, "Cavity-Backed Slot-Coupled Patch Antenna Array With Dual Slant Polarization for Millimeter-Wave Base Station Applications," *IEEE Antennas Propag. Mag.*, vol. 69, no. 3, pp. 1404–1413, 2021.

[27] D. A. Cahyasiwi, F. Y. Zulkifli, and E. T. Rahardjo, "Switchable Slant Polarization Filtering Antenna Using Two Inverted Resonator Structures for 5G Application," *IEEE Access*, vol. 8, pp. 224 033–224 043, 2020.

[28] X. Quan, R. Li, Y. Fan, and D. E. Anagnostou, "Analysis and Design of a 45° Slant-Polarized Omnidirectional Antenna," *IEEE Antennas Propag. Mag.*, vol. 62, no. 1, pp. 86–93, 2014.

[29] H. Kim, J. Kim, and J. Oh, "Communication A Novel Systematic Design of High-Aperture-Efficiency 2D Beam-Scanning Liquid-Crystal Embedded Reflectarray Antenna for 6G FR3 and Radar Applications," *IEEE Antennas Propag. Mag.*, vol. 70, no. 11, pp. 11 194–11 198, 2022.

[30] NR, "Base Station (BS) Conformance Testing Part 2: Radiated Conformance Testing (Release 15)," Technical Specification (TS) 38, 2018.

[31] Y. Zhu, A. R. Vilenskiy, O. A. Iupikov, P. S. Krasov, T. Emanuelsson, G. Lasser, and M. V. Ivashina, "A Varactor-Based Reconfigurable Intelligent Surface Concept for 5G/6G mm-Wave Applications," in *Proc. 18th Eur. Conf. Antennas Propag. (EuCAP)*, 2024, pp. 1–5.

[32] R. Maaskant, O. A. Iupikov, P. S. Krasov, R. Rehammar, A. A. Glazunov, and M. V. Ivashina, "A New Hybrid Chamber for Generating a Spectrum of Oblique Incident Plane Waves at the DUT," *IEEE Trans. Antennas Propag.*, vol. 69, no. 10, pp. 6806–6815, 2021.